

---

# Application of Phase Retrieval for Characterizing a High-Intensity Focused Laser Field

## Introduction

Focal-spot diagnostics (FSD's) for a high-intensity laser is one of the basic diagnostic requirements for analyzing high-field laser-matter interaction experiments. Many different parameters of a focal spot might be of interest to an experimenter—encircled energy per a given radius, the peak power density of a focal spot, the evolution of local hot spots along the propagation direction, or a full two-dimensional complex-field distribution for a more-comprehensive laser-matter interaction study. The difficulties of implementing focal-spot diagnostics for high-power lasers lie mostly in the necessity of devising an indirect technique because no instrument can survive direct measurements. The indirect technique, therefore, needs thorough qualification regarding how closely it is capable of representing real focal spots.

One of the appealing approaches to FSD is to measure near-field amplitude and phase to predict the field at the focus. This approach can determine the full complex-field distribution at any plane near the focus using well-known diffraction theories. In addition, the on-shot focal spot can be calculated easily without interfering with target experiments. Since the focal-spot is more affected by wavefront error than by fluence error, it is important that the wavefront error be minimized in this approach. One source of wavefront error is the non-common-path aberrations (NCPA's)—the difference between the measured wavefront through the sample beam path and the on-shot wavefront. We designate this difference as “transfer wavefront.” We also designate the aberrations belonging only to the diagnostic path as “intrinsic NCPA's” and the aberrations not captured by the diagnostic setup as “extrinsic NCPA's.” The transfer wavefront is obtained by subtracting the intrinsic NCPA from the extrinsic NCPA.

Transfer wavefront is characterized by sending probe beams through the optical beam path under consideration. There are, in general, two approaches for characterizing transfer wavefront depending on the arrangement of probe sources and the number of wavefront-measurement locations. In the first approach a single probe source, or so-called reference beam, is sent out

to characterize both intrinsic and extrinsic NCPA's; but the wavefronts are measured at two different locations: at the end of the diagnostic beam path and after the final focusing optic in the experimental chamber. This approach was demonstrated in a 100-TW class laser.<sup>1</sup> In the second approach, two probe sources are used at each end of the diagnostic and on-shot path and the wavefront is measured at only a single location, which is at the end of the diagnostic beam path. These two approaches are conjugate to each other in concept. For convenience the first approach is called single-source FSD or FSD-1, and the second is called double-source FSD or FSD-2.

Schematics for both versions of FSD are shown in Fig. 114.46. The on-shot wavefront is measured by a wavefront sensor located at a diagnostic table. The intrinsic NCPA's ( $W_i$ ) of the measured wavefront are the down-collimator aberrations and other aberrations in the optics located in the diagnostic table. The aberrations from the leaky mirror through the transport optics to the off-axis-paraboloidal (OAP) mirror are extrinsic NCPA's ( $W_e$ ). In FSD-1, the calibration source as noted in Fig. 114.46(a) is a low-energy reference beam co-propagating with the main beam. The wavefront of this reference beam is measured at the diagnostic table and in the target chamber. The wavefront at location  $W_2$  in the target chamber can be directly measured using a near-field imaging setup.<sup>1</sup> In our case, we chose to use a phase-retrieval method using multiple focal spots measured with a high-resolution focal-spot microscope (FSM) at different longitudinal locations.

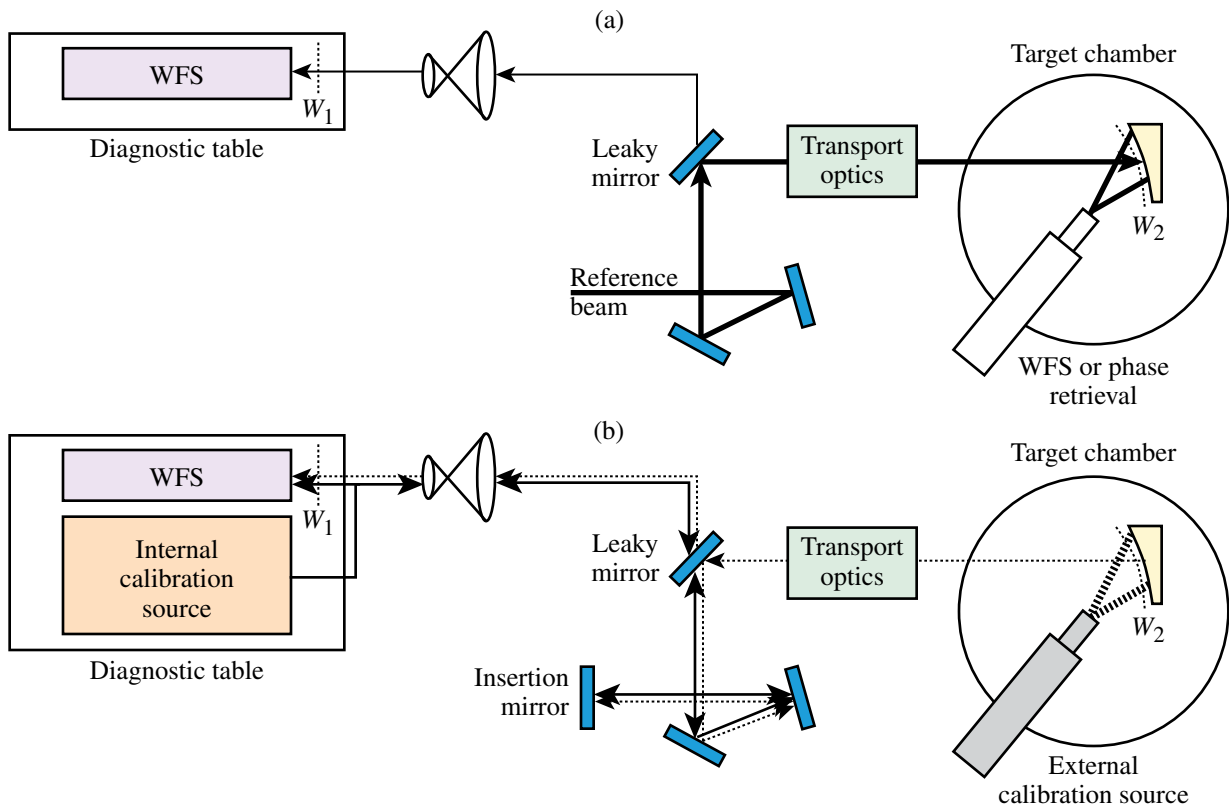
Using a reference beam, at  $W_1$ ,

$$W_{r1} = W_{\text{ref}} + W_i, \quad (1)$$

where  $W_{\text{ref}}$  is the aberrations in the reference beam itself before the leaky mirror and  $W_{r1}$  is the wavefront measured at the sensor location.

At  $W_2$ ,

$$W_{r2} = T(W_{\text{ref}} + W_e) - W_i, \quad (2)$$



E16590JRC

Figure 114.46

(a) FSD-1 uses one calibration source, and wavefronts are measured at two locations to calculate the transfer wavefront. (b) FSD-2 uses two calibration sources, and the wavefront is measured at only one location. WFS: wavefront sensor

where  $W_{r2}$  is obtained by the phase-retrieval method or by direct measurement.  $W_i$  is an instrument error either in the wavefront-sensor imaging system or in the focal-spot microscope used in the phase retrieval.  $T(\cdot)$  is a transformation function describing the spatial coordinate difference and the image distortion after the reflection off of the off-axis paraboloid.<sup>2</sup> For a large  $f$ -number focusing,  $T$  can be a simple linear transformation because the distortion is negligible.

The transfer wavefront is

$$W_{\text{transfer}} = W_e - W_i = T^{-1}(W_{r2} + W_t) - W_{r1}, \quad (3)$$

and the on-shot wavefront in the target chamber is calculated as

$$W_{2, \text{on-shot}} = W_{1, \text{on-shot}} + W_{\text{transfer}}. \quad (4)$$

The locations of  $W_1$  and  $W_2$  are shown in Fig. 114.46.

In the FSD-2 approach, the wavefront sensor located at the diagnostic table measures the intrinsic term, characterized by sending a source twice through the diagnostic path reflected

by a temporary insertion mirror [Fig. 114.46(b)]. Let us refer to this quantity as  $W_s$  and the source as the “internal calibration source.” If we send another source located at the center of the target chamber backward through the system, the extrinsic term as well as the intrinsic term will be detected at the sensor location. We denote this measured quantity as  $W_p$  and call the calibration source “external calibration source”:

$$W_s = W_{i,0} + 2W_i, \quad (5)$$

$$W_p = T^{-1}(W_{e,0}) + W_e + W_i, \quad (6)$$

where  $W_{i,0}$  and  $W_{e,0}$  are the aberrations that are inherent to the intrinsic and extrinsic calibration sources, respectively. Each has to be measured separately. The inverse transformation is needed to remap the extrinsic source error in a planar space, whereas it is not necessary to apply the inverse transformation to  $W_{i,0}$  because the internal calibration source is usually created by a simple on-axis beam collimator that does not distort the beam; it is easily measured by inserting an extra mirror close to the wavefront-sensor location.

The transfer wavefront is calculated as

$$W_{\text{transfer}} = W_e - W_i = (W_p - W_s) - [T^{-1}(W_{e,0}) - W_{i,0}]. \quad (7)$$

A concern with this calibration scheme is the necessity of using a high-power source during the measurement of  $W_s$  because of the energy loss associated with the double-pass transmission through the leaky mirror. The main signal might also suffer severe ghost reflections from other optics in the intermediate locations.

In either calibration procedure, the resulting transfer wavefront map should cover the on-shot main beam in the area for the calibration map to be meaningful. The advantage of FSD-2 is that beam registration is automatic and it is easy to subtract and add wavefronts from the internal or external source. However, in the presence of non-negligible aberrations in the external calibration source, the registration task becomes non-trivial and one might have to apply the distortion transformation. Also, the requirement that the two calibration beams should be co-propagating without a centering error poses some alignment challenges. FSD-1, however, has the advantage of being insensitive to the aberrations in the reference beam. It also allows a more direct adaptive-optic correction of the incoming beam as a whole due to the presence of a wavefront-sensing scheme after the final focusing optic.

OMEGA EP is a petawatt laser currently being built at LLE. The focal-spot diagnostics for OMEGA EP is based on the FSD-2 approach. Owing to the complexity of the system, there is always a risk that relying on only one approach might limit our capability to characterize the transfer wavefront under certain conditions. Along with the baseline OMEGA EP FSD development, we investigate the feasibility of implementing FSD-1, especially using a phase-retrieval method. In the **Phase-Retrieval Formalism** section that follows, the mathematical formalism of the phase-retrieval method will be discussed. In the **Off-line FSD Test-Bed Results** section (p. 97), the wavefronts at  $W_2$  obtained by FSD-2 and by the phase-retrieval FSD will be compared and shown to agree well with each other, thus confirming the phase-retrieval method. In the **FSD Demonstration in the MTW Laser System** section (p. 99), phase-retrieval FSD will be applied to predict a focal spot in the Multi-Terawatt (MTW) Laser System, which is compared with the direct focal-spot measurements.

Throughout this article the criterion of FSD accuracy is measured in terms of  $R_{80}$  error.  $R_{80}$  is an encircle radius that captures 80% of the total energy at the focus. Although the true  $R_{80}$  value is not known,  $R_{80}$  from a direct focal-spot measure-

ment is considered as the true  $R_{80}$  for the purpose of  $R_{80}$  error calculation. Currently OMEGA EP requires less than 10% error in  $R_{80}$  prediction.

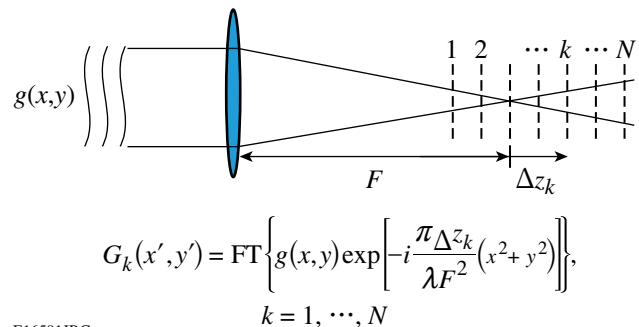
### Phase-Retrieval Formalism

Phase retrieval is a calculation technique that retrieves phase information from available intensity measurements that are connected by an integral or differential form of a propagation equation. A phase profile is sought that recreates all the measured intensity profiles under the propagation constraint. One can systematically find a solution using one of the search methods typically available from commercial optimization packages. In this section we describe a phase-retrieval method based on multiple near-focus measurements and one near-field fluence measurement. Increasing the number of measurement planes improves the accuracy of the result as well as the dynamic range of the retrieved phase.<sup>3</sup>

In Fig. 114.47, the measurement schemes and notations are described. A complex near field  $g(x,y)$  is focused by a focusing optic with a focal length of  $F$ . The focused intensity profiles are measured at  $N$  locations defocused from the focus by  $\Delta z_k$ . The complex field at the  $k$ th plane ( $G_k$ ) is calculated by the Fourier transform after multiplying  $g(x,y)$  with a defocusing term;  $g(x,y)$  is described by the measured near-field intensity  $I_0(x,y)$  and an unknown phase, which is to be retrieved. The phase term can be expressed as a sum of basis functions ( $\xi_n$ ) multiplied by modal coefficients  $a_n$ :

$$g(x,y) = \sqrt{I_0(x,y)} \exp\left[i \sum_n a_n \xi_n(x,y)\right]. \quad (8)$$

Here we chose to use modal expansion instead of a point-by-point phase representation. If the two-dimensional phase map is allowed to vary point by point, the retrieved phase is susceptible



E16591JRC

Figure 114.47

Phase retrieval using a multiple-focal-plane intensity measurement.

to discontinuities due to noise in the focal-spot measurements. A modal approach allows one to obtain a smooth phase map but sacrifices resolution for high-spatial-frequency terms not captured by the employed modes. The basis functions commonly used are Zernike polynomials for a circular beam shape or Legendre polynomials for rectangular shapes. For the actual laser beam, which is neither a perfect circle nor a rectangle, one chooses a circle or a rectangle whose size is just large enough to include the whole laser beam. The inner product, however, is defined only within the laser-beam boundary. As long as the beam shape is close to the ideal geometrical figure, this quasi-modal expansion closely represents the original surface.

The error metric to be minimized is

$$\varepsilon(\{a_n\}) = \sum_{k=1}^N \lambda_k \iint [ |G_k(x', y')| - \sqrt{I_k(x', y')} ]^2 dx' dy', \quad (9)$$

where  $\lambda_k$  is a weighting factor for the measurement plane  $k$ . Using the expression of the far field for the  $k$ th plane ( $G_k$ ), the error metric can be seen as a function of the modal coefficients  $a_n$ , where we search for a set of coefficients that minimize the magnitude of the error metric. Generally the searching process can be made more efficient when the gradients of the error metric with respect to each search variable are available as an analytic form.<sup>4</sup> In this case the gradient for the coefficient  $a_n$  is

$$\frac{\partial \varepsilon}{\partial a_n} = 2 \operatorname{Imag} \left\{ \iint \operatorname{IFT} \left[ \sum_{k=1}^N \lambda_k (G_k - \sqrt{I_k} e^{i\psi_k}) \right]^* \xi_n g \, dx dy \right\}, \quad (10)$$

where IFT is the inverse Fourier transform,  $\psi_k$  is the phase of the complex field  $G_k$ , and  $I_k$  is the measured intensity at the  $k$ th plane. The measured intensity usually contains noise that can be negative after background subtraction, so the negative values are set to zero. To measure focal spots, it is ideal to measure intensity by placing a CCD (charge-coupled device) camera directly at the focal planes; however, for low- $f$ -number focusing, a microscope imaging system is needed to resolve a small focal spot. For such a case, the aberrations in the microscope system should be negligible. The modal coefficients for tip and tilt terms are allowed to vary independently for each plane because the mechanical translation is not typically linear. That is, if the number of coefficients to be retrieved is  $M$ , the actual number of coefficients that are optimized is  $M + 2(N-1)$ .

With the error metric and the gradients given, a MATLAB<sup>®</sup> optimization routine (“fminunc”) is used to retrieve the modal coefficients. The routine uses a trust-region approach.<sup>5</sup> The

typical number of iterations for successful retrieval is less than 20, using five measurement planes.

### Off-line FSD Test-Bed Results

Before applying the phase-retrieval method in the MTW Laser System, it was first tested in an off-line FSD test bed where it is possible to compare a directly measured wavefront and a retrieved wavefront. The experimental setup is shown in Fig. 114.48. The setup is designed to mimic basic configurational features of OMEGA EP focal-spot diagnostics; it contains a wavefront sensor, a focal-spot microscope, transport optics, an OAP, down-collimation telescopes, a leaky mirror, and an insertion mirror as well as internal and external calibration sources [Fig. 114.46(b)]. The same wavefront sensor and focal-spot microscope were used in both the test-bed setup and the FSD demonstration in the MTW Laser System.

The wavefront sensor chosen for OMEGA EP is a Shack-Hartmann wavefront sensor—HASO—manufactured by Imagine Optic. It has a  $128 \times 128$  lenslet array with a  $14 \times 14$ -mm<sup>2</sup> CCD sensor area. The focal length of each microlens is 6.3 mm, which can measure local slopes up to 15 mrad. The accuracy of the defocus term was measured to be better than 0.01 waves at  $1.053 \mu\text{m}$ , and the relative error of astigmatism was found to be within 2%. Accuracy in higher-order aberrations was studied using custom-designed sinusoidal phase plates of one wave peak-to-valley. Wavefront measurements up to one quarter of the maximum spatial frequency were confirmed to be within less than 1% discrepancy with the interferometric measurements. Measurements at higher spatial frequency with the reference phase plates were limited by the maximum slope limit of the sensor.

The prototype FSM consists of a high-quality microscope objective (Mitutoyo,  $10\times$ , N.A. = 0.26, nominal focal length = 20 mm), a tube lens (nominal focal length = 200 mm), and a scientific-grade, 16-bit CCD camera (SI-800, Spectral Instruments). The microscope objective has a long working distance suitable for high-fluence measurements. The objective is infinity corrected, so a tube lens refocuses the image at the CCD. The actual dynamic range of the camera is reduced to 14 bits due to read noise. The camera was cooled at  $-35^\circ\text{C}$  in all cases to minimize noise.

The thick black line in Fig. 114.48 represents the main beam line.  $W_s$  is measured by the external calibration source placed at the FSM image plane, and  $W_p$  is measured by the internal calibration source placed next to the wavefront sensor.  $W_2$  is calculated according to Eq. (4). All the calibration beams and

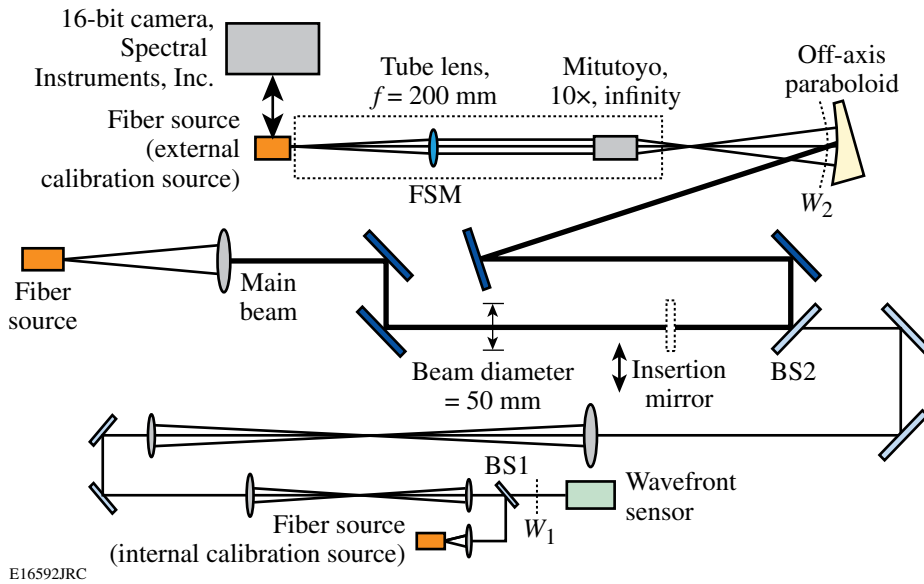
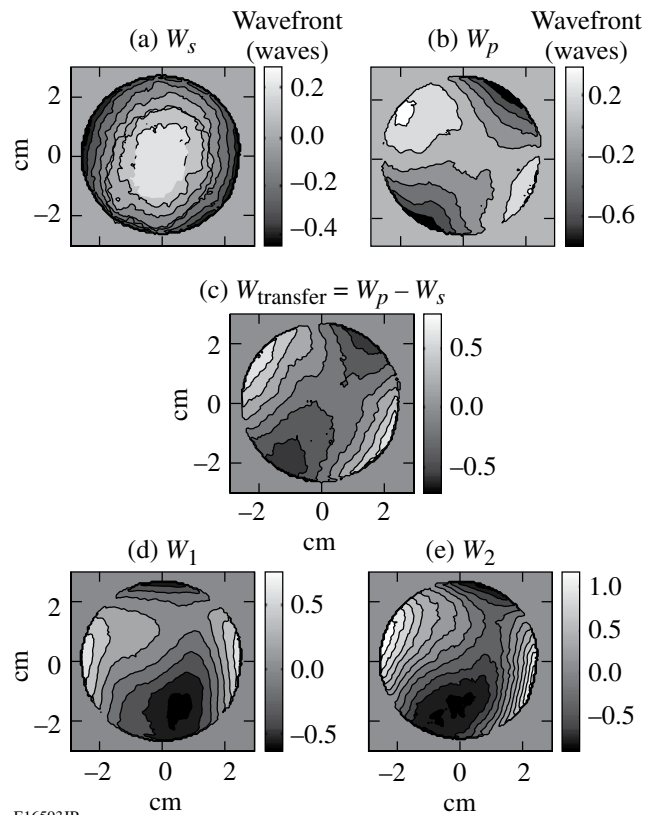


Figure 114.48  
The test-bed setup with a geometry similar to the OMEGA EP FSD setup. BS: beam splitter; FSM: focal-spot microscope unit.

the main beam source are obtained from collimating the diverging beam from a single-mode fiber tip injected with a 1053-nm continuous-wave laser. The main beam is a 2-in.-diam round beam down-collimated at the sensor location by a factor of 5. The beam is attenuated before the fiber sources so there are no filter-induced aberrations in the setup. The whole setup was covered with acrylic glass to prevent measurement corruption from air turbulence. The lenses in the two down-collimators and the collimator lens for the main beam were intentionally tilted to introduce aberrations. The main beam is focused by a 200-mm effective-focal-length OAP mirror and the focus is imaged to the FSM.

Figure 114.49 summarizes the wavefronts measured by the FSD-2 procedure. The measured and the calculated focal spots are also shown in Fig. 114.50. The fine details of the calculated focal spot are in excellent agreement with those of the measurement, but the relative  $R_{80}$  discrepancy (12%) slightly exceeds the OMEGA EP accuracy requirement (10%) at the best-focus position [Fig. 114.50(d)].  $R_{80}$  errors for five different focal spots measured at  $\Delta z = -500, -250, 0, 250,$  and  $500 \mu\text{m}$  are  $-2.1, -5.4, -12, -6.2,$  and  $2\%$ , respectively. It appears that this discrepancy in  $R_{80}$ , which is more pronounced near the best-focus position, actually results from an incoherent background halo in the FSM measurements,<sup>6</sup> which spreads focused light away from the center of focus.

With the direct characterization of wavefront using the FSD-2, we can compare this with the retrieved wavefront from the multiple focal plane phase-retrieval method, which uses the aforementioned five focal-spot measurements. The best-fitting



E16593JR

Figure 114.49  
Summary of wavefront measurements in the test-bed setup. (a)  $W_s$ , (b)  $W_p$ , (c)  $W_{\text{transfer}}$ , and (d) a wavefront measured at the wavefront sensor location ( $W_1$ ), and (e) a calculated wavefront after the paraboloidal mirror ( $W_2 = W_1 + W_{\text{transfer}}$ ). The wavefront units are in waves.

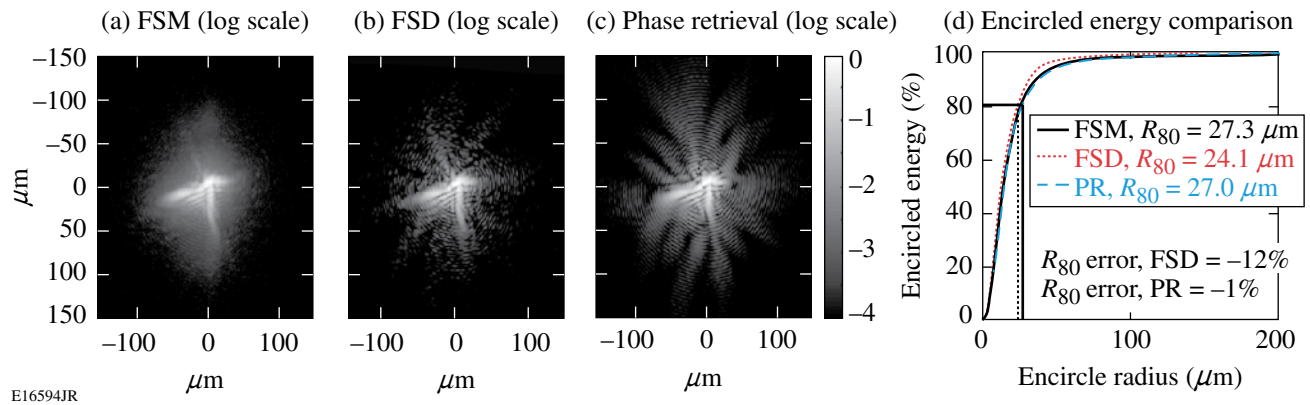
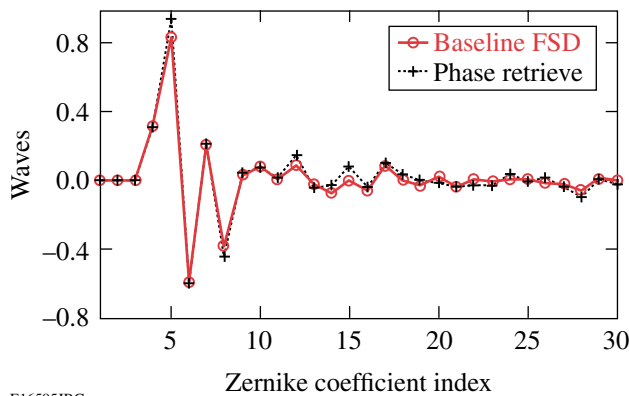


Figure 114.50

The calculated and measured focal spots for the test-bed experiment. (a) Directly measured focal spot by FSM, (b) calculated focal spot based on FSD calibration, (c) calculated focal spot from the retrieved Zernike coefficients, and (d) encircled energy comparisons and the relative  $R_{80}$  errors with respect to the  $R_{80}$  value of the directly measured focal spot.

Zernike coefficients that minimize the difference between the measured and the calculated focal spots are calculated by an optimization routine. The retrieved wavefront, corresponding to  $W_2$ , agrees well with the  $W_2$  from the baseline FSD. Figure 114.51 compares Zernike coefficients and the wavefront difference. The rms (root-mean-square) difference between the two wavefronts is 0.074 waves. Although one might expect that the  $R_{80}$  prediction from the retrieved phase coefficients would have similar errors as in the FSD-2 approach, the  $R_{80}$  errors in the five different focal planes in the phase-retrieval case are actually all within 2%. Putting more weight on the direct measurements, it shows that it is possible for the phase-retrieval process to produce a wavefront map that fits all the focal-spot



E16595JRC

Figure 114.51

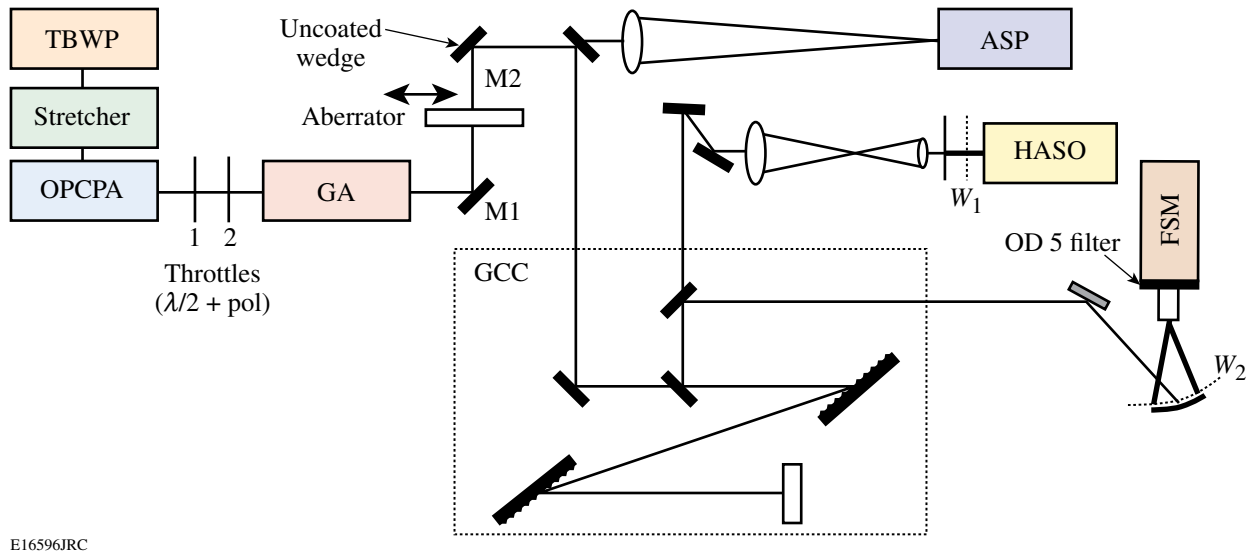
Zernike coefficients from the FSD calibrated wavefront and from phase retrieval from multi-focal-plane data agree well with each other. The rms wavefront difference is 0.074 waves.

data while still being slightly off from the true wavefront. Throughout this experiment the external and internal source errors were assumed negligible; also, the distortion mapping was not applied because the  $f$  number ( $\sim 4$ ) is relatively large.

#### FSD Demonstration in the MTW Laser System

The MTW FSD setup (Fig. 114.52) is based on phase-retrieval FSD (FSD-1) because an external calibration source is not available in the target chamber. In this case the pulse energetics is a practical concern. The attenuation was prepared in three steps; first through wave plates and a polarizer, second by Fresnel reflection off an uncoated wedge (M2), and finally by neutral-density filters inside the FSM. The main glass amplifier was not fired throughout the experiment.

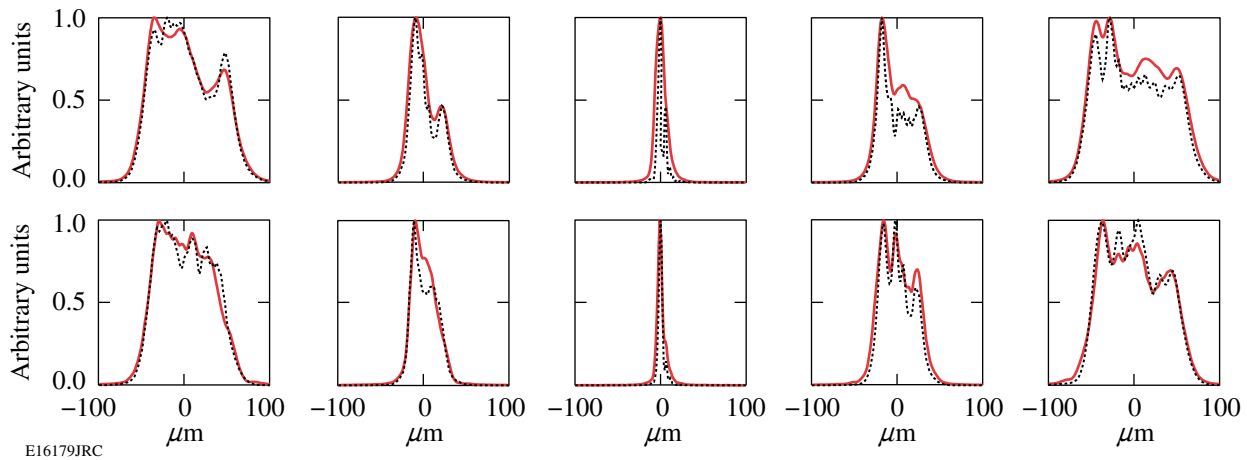
Similar to the FSD test-bed case, the beam is focused by an  $f/4$  off-axis paraboloidal mirror; we measured focal spots at five different planes near focus separated by  $250 \mu\text{m}$ . The objective was mounted on a remotely controlled translation stage for operation under vacuum, and the position of the objective was optically monitored using a target-viewing system. We obtained a set of modal phase coefficients that minimize an error metric, which quantifies the difference between the measured data and the intensity computed from the phase estimate, by an optimization routine under the assumption that the field is monochromatic. The modal basis is represented by Legendre polynomials because the beam shape is close to square. Figure 114.53 shows lineout comparisons at each plane after completion of the algorithm. We note generally good agreement in every plane except at the focused plane (first row, third column); the blurring of the focal spot in the horizontal direction is due to angular dispersion caused by a



E16596JRC

Figure 114.52

Experimental setup for a phase-retrieval FSD demonstration in the MTW Laser System. TBWP: a mode-locked oscillator; OPCA: parametric amplifier; GA: 15-cm-thick glass amplifier (inactive); HASO: wavefront sensor; ASP: pointing sensor; GCC: compressor chamber; FSM: focal-spot microscope.



E16179JRC

Figure 114.53

Horizontal (first row) and vertical (second row) lineout comparisons at each plane. The solid lines are from measurements; the dashed lines are from the phase-retrieval calculations. Distances are 500, 250, 0, -250, and -500  $\mu\text{m}$  from the left column to the right.

slight misalignment of the compressor gratings. The angular dispersion was independently measured to be  $47 \mu\text{rad}$  over the 7-nm bandwidth by marking the bandpass-filtered focal-spot position change from 1050 nm to 1057 nm. Therefore we find it better to exclude the zero-defocus plane measurement in the search algorithm. On the other hand, the focus plane measurement can be used to estimate the amount of angular dispersion. The amount of angular dispersion estimated from phase-retrieval results is  $50 \mu\text{rad}$ , which agrees with the independently measured value within 7% relative error.

Once the wavefront of the focusing beam is successfully characterized, this information can be used to characterize focal spots at higher energies by separately measuring the differential wavefront change. As shown in Fig. 114.54, the wavefront sensor on the diagnostic table measures sets of wavefronts belonging to the same beam used in the phase retrieval. The transfer wavefront is calculated according to Eq. (7) [Fig. 114.54(c)]. With the transfer wavefront quantified, the characterization of focal-spot distribution under a different circumstance should be possible by a single wavefront

measurement at the diagnostic table. To validate this idea, an aberrated, transmissive element was placed before the leaky mirror (Fig. 114.52). The directly measured focal spot [Fig. 114.55(a)] morphologically agrees well with the predicted focal spot using the wavefront of Fig. 114.54(e) as shown in Fig. 114.55(b), whereas the agreement is poor without using the transfer wavefront [Fig. 114.54(d) and Fig. 114.55(c)]. The calculated and directly measured focal spots are also compared in logarithmic scale in Figs. 114.56(a) and 114.56(b). The  $R_{80}$  error [Fig. 114.56(c)] is 13%, which falls slightly short of the OMEGA EP requirement. The encircled energy of the FSM focal spot shows that it has more energy scattering beyond  $R_{80}$  than FSD test-bed measurements; this may result from the extra use of filters in the FSM for attenuating the beam.

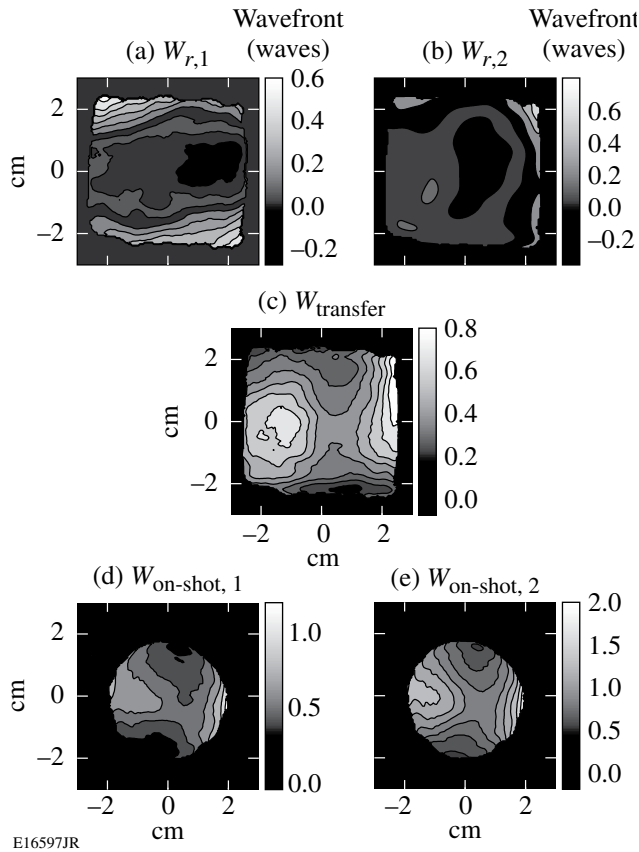
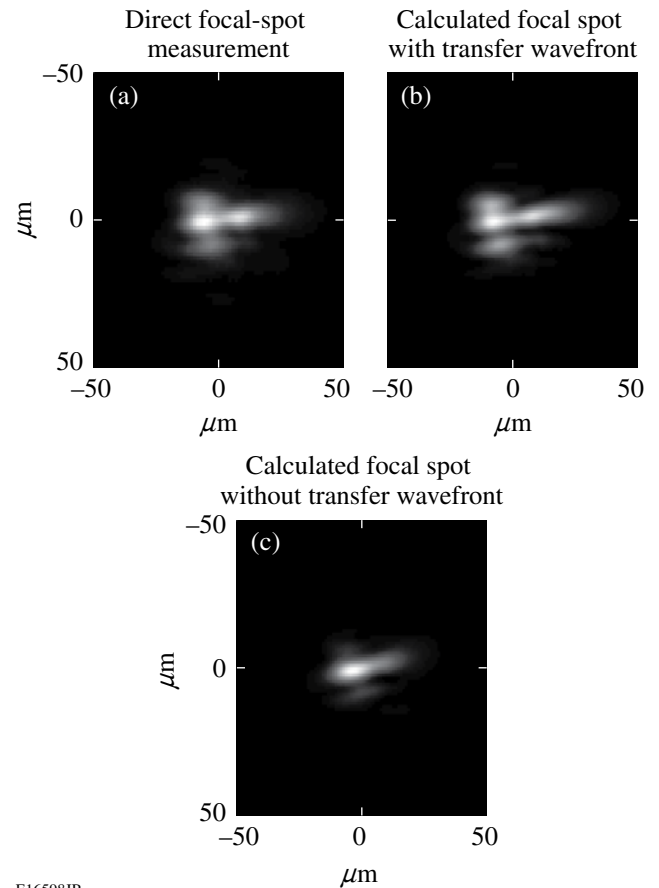


Figure 114.54 Wavefront summary of an OPCPA laser beam. (a) Wavefront measured at the wavefront sensor location, (b) wavefront after OAP reflection, from phase retrieval, (c) transfer wavefront [Eq. (3)], (d) wavefront measured at the wavefront sensor location after the insertion of an aberrator, and (e) calibrated wavefront for the  $W_2$  plane using the transfer wavefront. Wavefront unit is in waves.

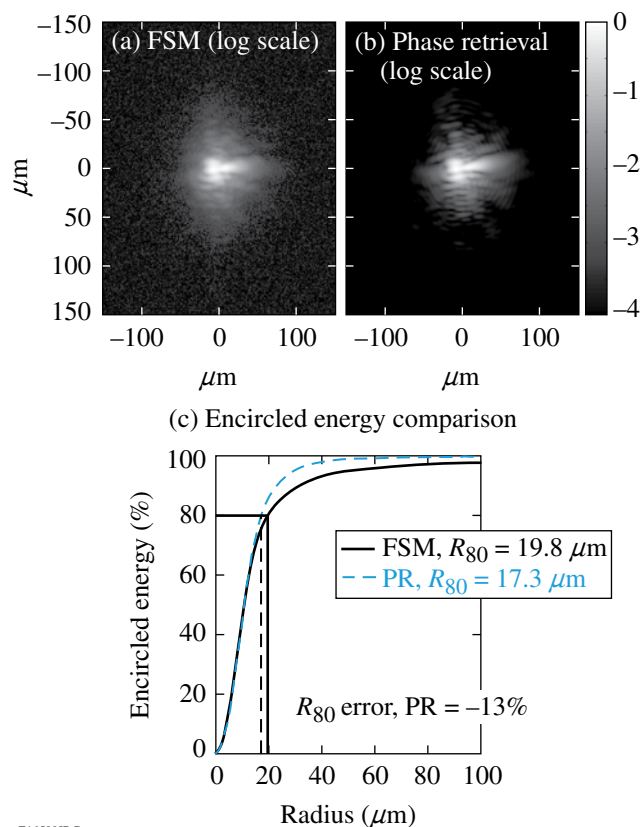


E16598JR

Figure 114.55 Linear scale comparison of the directly measured focal spot (a) in the presence of an aberrator with the calculated focal spot, (b) using the transfer wavefront obtained from phase retrieval, and (c) not using the transfer wavefront.

### Conclusions

This work presented focal-spot diagnostic concepts for a high-power laser system, which is based on measuring a near-field complex field for predicting a far field. Since the wavefront at the target chamber is not directly measurable, we demonstrated two calibration procedures to characterize a “transfer wavefront” with which the measured wavefront at the diagnostic table can be easily converted to the actual wavefront at the target chamber location. One FSD approach (FSD-2) is based on direct wavefront measurements using multiple calibration sources, whereas the phase-retrieval FSD (FSD-1) is based on phase retrieval using multiple focal-plane measurements. The two calibration methods were successfully demonstrated in the FSD test-bed setup. The test-bed results show that phase retrieval agrees with the direct measurement within 0.07 waves rms. In the MTW system, the phase-retrieval FSD was applied to characterize the transfer wavefront and a focal



E16599JRC

Figure 114.56

Logarithm scale comparison of the directly measured focal spot (a) in the presence of an aberrator with the calculated focal spot and (b) using the transfer wavefront obtained from phase retrieval. Encircled energy comparisons (c) show 13% of relative  $R_{80}$  error.

spot. The disagreement in  $R_{80}$  seen in both the test-bed setup and the MTW system suggests that the FSM data may have been corrupted by an incoherent background halo. Currently the  $R_{80}$  error is not smaller than 10% from the experimental verification point of view. On the other hand, the availability of the phase-retrieval technique will complement the application of the baseline FSD in OMEGA EP, which might be impaired by system complexity.

#### ACKNOWLEDGMENT

The authors thank J. R. Fienup for helpful discussions and G. R. Brady for help with numerical implementations. This work was supported by the U.S. Department of Energy Office of Inertial Confinement Fusion under Cooperative Agreement No. DE-FC52-08NA28302, the University of Rochester, and the New York State Energy Research and Development Authority. The support of DOE does not constitute an endorsement by DOE of the views expressed in this article.

#### REFERENCES

1. S.-W. Bahk, P. Rousseau, T. A. Planchon, V. Chvykov, G. Kalintchenko, A. Maksimchuk, G. A. Mourou, and V. Yanovsky, *Opt. Lett.* **29**, 2837 (2004).
2. S.-W. Bahk, P. Rousseau, T. A. Planchon, V. Chvykov, G. Kalintchenko, A. Maksimchuk, G. A. Mourou, and V. Yanovsky, *Appl. Phys. B* **80**, 823 (2005).
3. V. Yu. Ivanov, V. P. Sivokon, and M. A. Vorontsov, *J. Opt. Soc. Am. A* **9**, 1515 (1992).
4. J. R. Fienup, *Appl. Opt.* **32**, 1737 (1993).
5. T. F. Coleman and Y. Li, *SIAM J. Optim.* **6**, 418 (1996).
6. G. Kuwabara, *J. Opt. Soc. Am.* **43**, 53 (1953).